RSC Advances

PAPER

View Article Online
View Journal | View Issue

Cite this: *RSC Adv.*, 2024, **14**, 14523

A novel layered double hydroxide-based ternary nanocomposite for the effective photocatalytic degradation of rhodamine B

Nader M. Abdelbar, *[ab] Mohamed A. Ahmed[a] and Ashraf A. Mohamed [a]

Photocatalytic degradation of organic pollutants is a green and effective route of wastewater treatment. Zinc oxide was initially used for this purpose; however, calcined zinc/chromium layered double hydroxide (ZnCr-LDO) and cadmium sulfide quantum dots (CdSQDs)-based nanocomposites proved as superior alternatives. Herein, we report a green sonochemical method for the sol–gel fabrication of novel CdSQDs@ZnCr-LDO/ZnO ternary nanocomposite that exhibited exceptional photocatalytic activity for the degradation of rhodamine B dye (RhB), in wastewaters, under UV-A-irradiation. The features of the ternary nanocomposite were investigated using various physicochemical techniques, including XRD, SEM, TEM, EDX, XPS, BET, zeta potential, DRS, and PL measurements. The RhB dye % removal was 38.02, 40.2, and 98% using pristine ZnO, ZnCr-LDO and the ternary CdSQDs@ZnCr-LDO/ZnO-based nanomaterials, respectively, reflecting the superior ternary nanocomposite's photocatalytic activity that made it an excellent competitor to commonly reported photocatalysts. Additionally, an investigation was carried out to determine the key reactive species in the photocatalytic degradation of RhB, considering both scavenger's type and concentration. The prevailing mechanism was found to be the reductive photodegradation pathway. Furthermore, several models were utilized to describe the kinetics of photocatalytic performance of the ternary nanocomposite and a typical Z-scheme type-II photocatalytic heterojunction mechanism was inferred.

Received 26th January 2024
Accepted 27th April 2024

DOI: 10.1039/d4ra00685b

rsc.li/rsc-advances

1. Introduction

Organic pollutants, such as dyes, in wastewater pose a major threat to ecosystems and aquatic life.[1–4] Pharmaceutical, textile, cosmetics, food, paint, ceramics, and pigment industries utilize dyes to color their products.[1–3] Among dye pollutants, RhB dye is a stable xanthene dye commonly used in the laboratory as a stain tracer to determine the direction and rate of transport. Therefore, a suitable treatment should be established before discharging dye effluents to the water stream. To date, various techniques have been documented for eliminating RhB from aqueous solutions,[1–3] including advanced oxidation,[5] adsorption,[6] ionizing radiation,[7] ion exchange,[8] among other methods. However, achieving the removal of RhB at low concentrations is a difficult and challenging task.[9] Therefore, finding an eco-friendly, and cost-effective method is essential for treating waste-effluents containing low levels of RhB. On the other hand, photocatalytic degradation of organic pollutants is an effective effluent's remediation strategy that found widespread application.[2,10] In this regard, novel, effective, recyclable, eco-friendly and cost-effective photocatalysts are highly desirable. Various semiconductor materials, for instance ZnO, TiO_2, SnO_2, $SrTiO_3$, and CdS exhibited promising photocatalytic activities.[2,11] In practical context applications, the creation and design of semiconductor photocatalysts powered by visible/UV-A light, featuring appropriate band gap energies, remain crucial and present a significant challenge for researchers.[12,13] Therefore, extensive efforts is being exerted to assess the conversion capacities and light harvesting of various photocatalytic nanomaterials in the visible/UV-A range of the spectrum,[14] where improved photocatalysts were acquired by structural and compositional modification of pristine semiconductors.[2,15] Recently, different metal hydroxides M-OH, especially layered double hydroxides (LDH) and their calcined counterparts (LDO), have been examined as adsorbents and photocatalysts for the elimination and photo decomposition of organic pollutants, along with H_2-production purposes.[1,16,17] LDH-based materials are anionic clays, with the general formula $[M_{(1-x)}{}^{2+}M_{(x)}{}^{3+}(OH^-)_2]^{x+}[(X^{n-})_{(x/n)}\cdot mH_2O]^{x-}$, where M^{2+} and M^{3+} are divalent and trivalent metal ions, respectively, which have been abundantly studied for their catalytic activity[18] adsorption/separation,[19] biotechnology,[20] biomedical,[21] and other applications.[1] Recent progress in LDH-based photocatalysts has led to enhanced visible light harvesting, improved charge separation,

[a]*Chemistry Department, Faculty of Science, Ain-Shams University, Abbassia, Cairo-11566, Egypt. E-mail: nadermostafa_p@sci.asu.edu.eg; nadermostafa88@nhe.edu.eg; Tel: +2 01093730196*

[b]*Higher Institute of Engineering, Automotive Technology and Energy, New Heliopolis, Cairo, Egypt*

increased surface area, and better pollutant removal. This is achieved through band structure engineering, morphological control, and surface modifications; nevertheless, more focus is required on facile and up-scalable synthesis and suitability for sustainable industrial applications.[1–3]

Herein, a novel CdSQDs@ZnCr-LDO/ZnO ternary nanocomposite was synthesized, thoroughly characterized, and conveniently applied to the photocatalytic degradation of RhB. The influence of operating parameters including catalyst dose, initial dye concentrations, contact time, temperature, and pH on the photodegradation of RhB was evaluated. The kinetics and mechanism of dye photodegradation were explored.

2. Experimental

2.1 Materials

All chemical substances were procured from Sigma-Aldrich (St. Louis, MO, USA). Bi-distilled water was used throughout.

2.2 Instruments

The rate of photocatalytic degradation was monitored, in 10 mm cells, using a Shimadzu-1650-UV-visible spectrophotometer (Kyoto, Japan) that is controlled by UV-probe 2.5 software.[22] The pH measurements were conducted using a calibrated Adwa pH mV^{-1}, meter model 1000 (Szeged, Hungary). Centrifugation was conducted using an NF815 centrifuge (Ankara, Turkey). XRD measurements were performed with XRD-6100 X-ray diffractometer in a 2θ range of 5–70° using continuous scanning mode. HR-TEM JEOL 6340 electron microscope was utilized for imaging. The photocatalytic activity of synthesized catalyst was examined by following the RhB photodegradation under different light sources of Fluorescent white Lamp (2 × 15 W, 380–680 nm, 725 lm, Philips, Egypt), UV-A lamp (20 W, 368 nm, Sylvania, Germany), and UV-C lamp (20 W, 254 nm, Philips, Netherlands).

2.3 Fabrication of zinc oxide nanoparticles ZnO (NPs)

Zinc oxide nanoparticles were synthesized using a sol–gel method. A 20.0 g $Zn(NO_3)_2 \cdot 6H_2O$ were dissolved in 200 mL distilled water (DW), a 20 mL of 5% w/v aqueous pluronic-P123 was added as a polyol surfactant solution and capping agent under continuous stirring at 700 rpm, and the pH was adjusted to 9.0 ± 0.2 with 2.0 M ammonium hydroxide, at room temperature to form a milky $Zn(OH)_2$ based-sol–gel Then, the formed gel was allowed to age for a period of 24 hours, filtered, Subjected to drying at 110 °C and calcination at 450 °C for 3 h, grinded well, and sieved to give ZnO NPs as illustrated in Fig. 1a.

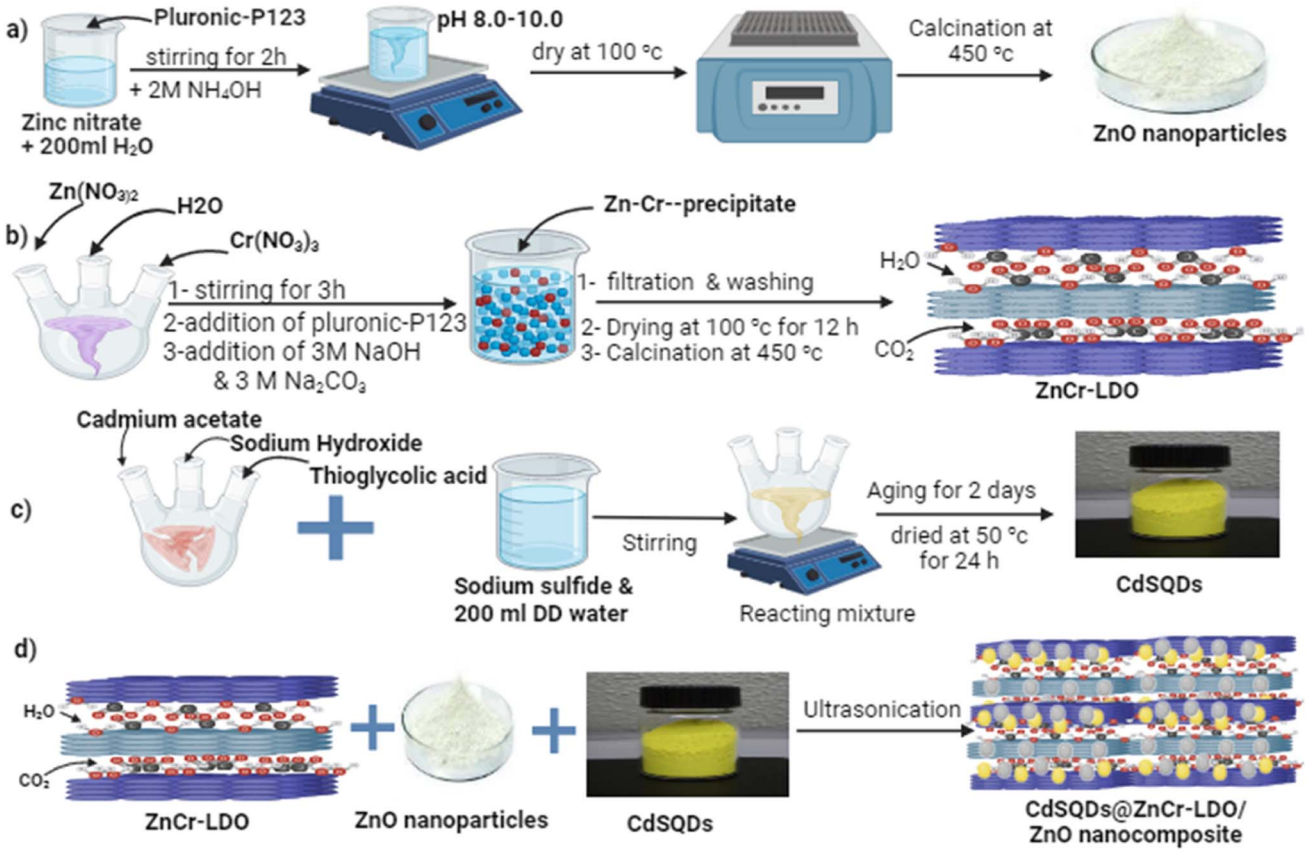

Fig. 1 Schematic diagram of synthesis method of (a) ZnO NPs, (b) binary ZnCr-LDO nanosheets, (c) CdSQDs, and (d) the ternary CdSQDs@ZnCr-LDO/ZnO nanocomposite.

2.4 Synthesis of ZnCr-LDO nanosheets

A mixture of 5.95 g $Zn(NO_3)_2 \cdot 6H_2O$, and 4.0 g $Cr(NO_3)_3 \cdot 9H_2O$, was dissolved in 200 mL of DW. This solution has a mole ratio of 2 : 1. A 20 mL of 5% w/v aqueous pluronic-P123 solution was added dropwise with stirring at 700 rpm, Fig. 1b. The pH was adjusted to 9.0 ± 0.2 by dropwise addition of a mixture containing 3.0 M NaOH and 2.5 M Na_2CO_3, serving as the intercalated anion between layers, where ZnCr-LDH was formed. The obtained LDH is left aside for 24 h, filtered off, washed with DW, dried, and calcined at 450 °C for 3 h to furnish the ZnCr-LDO nanosheets (ZnCr-LDO NSs).

2.5 Synthesis of cadmium sulfide quantum dots (CdSQDs)

CdSQDs was prepared as described previously.[23] Briefly, 0.70 g cadmium acetate was dissolved in 200 mL water, and a 2.0 mL thioglycolic acid was added as a thiol stabilizer and capping agent. The mixed solution's pH was adjusted to 12.0 ± 0.2 through the addition of 1.0 M NaOH, and stirred for two hours. Then a 0.24 g Na_2S was dissolved in 200 mL water, added dropwise with stirring to the previous solution and set aside for two days at room temperature, Fig. 1c. The settled down CdSQDs were separated, afterward, rinsed several times with absolute ethanol and dried at 50 °C for 24 h.

2.6 Synthesis of novel CdSQDs@ZnCr-LDO/ZnO ternary nanocomposite

The ternary CdSQDs@ZnCr-LDO/ZnO was synthesized in a mass ratio of 1 : 9 : 90 for CdSQDs: ZnCr-LDO NSs: ZnO NPs. Typically, a 0.18 g ZnCr-LDO and 1.80 g ZnO were dispersed together in 200 mL water in an ultrasonic bath for 3 h. After that, the powder was gathered through filtration, dried at 100 °C for a period of 3 h and denoted as the binary ZnCr-LDO/ZnO. Then, 0.02 g CdSQDs was dispersed over the surfaces of the binary ZnCr-LDO/ZnO by ultrasound irradiation, in 200 mL water, at room-temperature for 3 h. The formed powdered CdSQDs@ZnCr-LDO/ZnO ternary nanocomposite was collected by filtration and dried at 80 °C overnight, as depicted in Fig. 1.

2.7 Photocatalytic measurements

To evaluate the photocatalytic efficiency of the ternary CdSQDs@ZnCr-LDO/ZnO nanocomposite, aqueous RhB was employed as a typically highly stable model organic dye pollutant, under UV-A light irradiation. RhB has a maximum visible light absorption at 554 nm. Photocatalytic experiments were conducted in a homemade closed box with a 20 W, UV-A lamp as a source of UV-A light (368 nm), at room temperature. A 100 mL solution of 1.0 mg L^{-1} aqueous RhB dye was mixed with 10.0 mg of the ternary CdSQD@ZnCr-LDO/ZnO nanocomposite photocatalyst and stirred with the magnetic stirrer, for 1 h in the dark to allow attainment of adsorption equilibrium between the ternary nanocomposite photocatalyst and the adsorbate RhB dye, after that the UV-A lamp was turned on for $2\frac{1}{2}$ h. At pre-selected time intervals, 5.0 mL sample aliquots were withdrawn centrifuged, and the supernatant solution was transferred to a 10 mm spectrophotometric cell to record the RhB dye absorption spectrum against water as a reference.

3. Results and discussion

The current work describes a facile, straightforward, easily scalable, and cost-effective synthesis of CdSQDs/ZnCr-LDH/ZnO ternary nanocomposite photocatalyst and its precursors. ZnO nanoparticles were synthesized using a sol–gel method that provides control over nanoparticle size and morphology while being an environmentally benign method. ZnCr-LDH nanosheets were synthesized utilizing a simple co-precipitation method in the presence of CO_32- as an intercalating anion between the LDH layers. The sonochemical perturbation yielded smaller sized CdSQDs with a huge surface area, uniform dispersion and deposition, and anchoring onto the ZnCr-LDH nanosheets and ZnO NPs. Furthermore, ultrasound irradiation generates acoustic cavitation, which allows for the homogeneous distribution and strong binding of CdSQDs to LDH and ZnO NPs, resulting in synergistic effects that boost the overall photocatalytic activity.

3.1 Fourier-transform infrared spectroscopy (FTIR)

FTIR is a widely used technique to characterize the structural and bonding properties of materials by probing the modes of chemical bonds. The typical FTIR spectra of ZnO NPs shows a broad absorption band around 3400–3500 cm^{-1} corresponding to the stretching vibrations of O–H groups, indicating the presence of surface-adsorbed water or hydroxyl groups. The band around 1620 cm^{-1} is attributed to the bending vibrations of adsorbed water molecules. Bands in the fingerprint region (500–1300 cm^{-1}) is associated with the Zn–O stretching and bending vibrations, characteristics of the ZnO lattice, as shown in Fig. 2a, c and d. The FTIR spectra CdSQDs, Fig. 2b and d, exhibited bands related to the stretching and bending vibrations of functional groups of the capping agent, thioglycolic acid, such as O–H (3375.4 cm^{-1}), $-CH_3$ (2912.9 cm^{-1}), C=O (1629.5 cm^{-1}), and S–H bonds (2550 cm^{-1}, strongly weakened due to bonding with metal ions). Bands associated with the Cd–S stretching vibrations (778.7 cm^{-1}), although these may be less prominent due to the small size of the QDs Fig. 2b. Moreover, the FTIR spectra ZnCr-LDO NSs, Fig. 2c and d, showed bands at 799 and 952 cm^{-1} related to the vibrations of metal–oxygen bonds (Zn–O, Cr–O) in the layered structure. The wideness of the band indicates the existence of hydrogen bonds. The weak peak at 1635.7 cm^{-1} is attributed to the deformation vibration of interlayer water. Bands corresponding to the interlayer anions or guest species present between the LDO layers, *e.g.* carbonates. Furthermore, the ternary nanocomposite FTIR spectrum exhibited characteristic bands related to the individual components CdSQDs, ZnCr-LDO, and ZnO; however, with slight shifts or changes in the positions and intensities of these characteristic bands, indicating potential interactions or chemical modifications between the individual components, as shown in Fig. 2d.

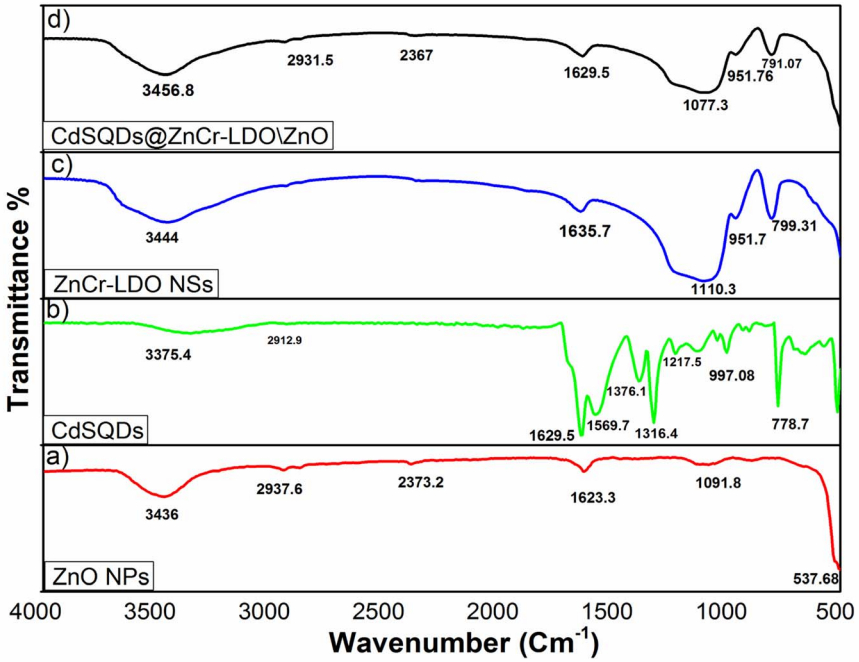

Fig. 2 FTIR spectra for (a) ZnO NPs, (b) CdSQDs, (c) ZnCr-LDO NSs and, (d) CdSQDs@ZnCr-LDO/ZnO ternary nanocomposite.

3.2 Crystallite properties

X-ray diffraction (XRD) is an effective tool that is customarily utilized in the characterization of nanomaterials to evaluate its crystallite features, including the crystal structure, average crystallite size, crystalline phases, and lattice parameters. Fig. 3 illustrates the XRD patterns of the prepared ZnCr-LDO, CdSQDs, ZnO, and CdSQDs@ZnCr-LDO/ZnO nanocomposite. The XRD pattern of the as-fabricated ZnCr-LDO, illustrated in

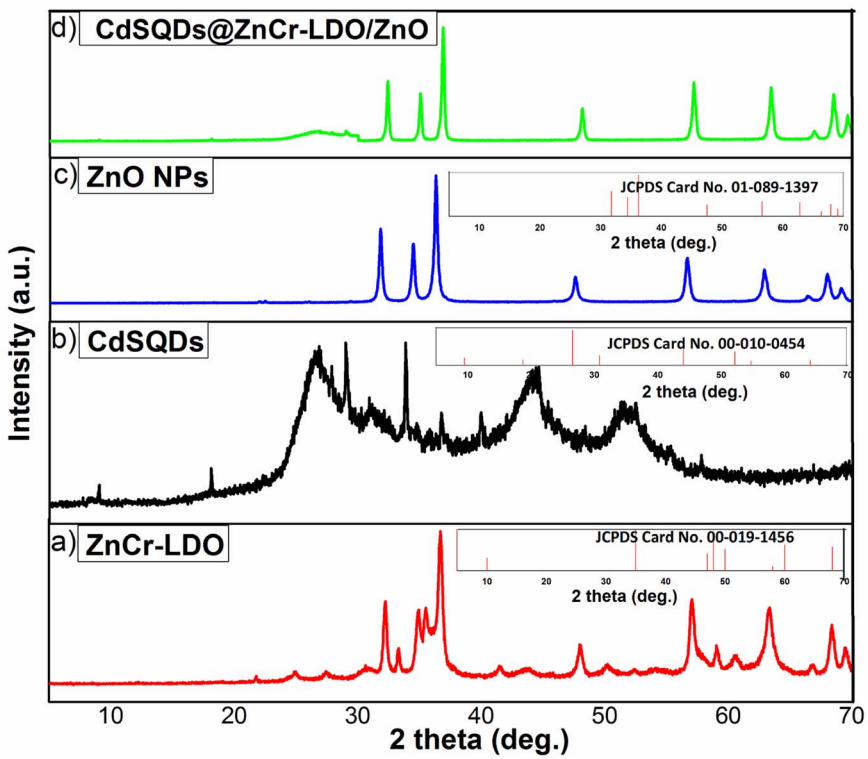

Fig. 3 XRD spectra of (a) ZnCr-LDO, (b) CdSQDs, (c) ZnO NPs, and (d) CdSQDs@ZnCr-LDO/ZnO nanocomposite.

Fig. 3a, confirmed its layered structure, as specified by diffraction peaks at 30.5°, 35.89°, 37.44°, 43.69°, 54.23° and 57.55° that are in harmony with JCPDS Card No. 00-019-1456.The fabricated CdSQDs exhibited broad XRD peaks at $2\theta = 26.7°$, 44° and 51.5°, as shown in Fig. 3b, corresponding to the crystalline planes 111, 200, and 311, respectively, with average size of 3.7 nm indicating a face centered cubic pattern (JCPDS Card No. 00-010-0454).

Moreover, the hexagonal wurtzite structure of the fabricated ZnO nanoparticles with space group $P6_3mc$ and crystallographic parameters $a = 3.253$ Å, $b = 3.253$ Å and $c = 5.213$ Å is in harmony with JCPDS Card No. 01-089-1397. These results demonstrated a high purity level of ZnO NPs fabrication possessing an average crystallite size of 40 nanometers. Furthermore, the XRD pattern of the as-fabricated CdSQDs@ZnCr-LDO/ZnO ternary nanocomposite, shown in Fig. 3d, exhibited all characteristic peaks of its individual components and showed an average crystal size of 36.6 nm, as calculated by Scherrer's equation and is in harmony with high resolution transmission electron microscopy (HR-TEM) findings, *vide infra*.

3.3 Morphological properties

The field emission scanning electron microscopic (FESEM) images of CdSQDs@ZnCr-LDO/ZnO nanocomposite are shown in Fig. 4. The SEM images (Fig. 4a and b) reflect the homogeneous deposition of CdSQDs onto ZnCr-LDO sheets and ZnO NPs surfaces. This uniform deposition demonstrated the effectiveness of the ultrasonic-assisted agitation in producing the ternary nanocomposite, CdSQDs@ZnCr-LDO/ZnO, where CdSQDs were uniformly dispersed throughout the structure of the hexagonal wurtzite configuration of ZnO nanoparticles and ZnCr-LDO nanosheets. Furthermore, the EDX, elemental overlay and mapping spectra for CdSQDs@ZnCr-LDO/ZnO nanocomposite comprised five primary components, including: O, S, Cd, Cr and Zn, with wt% 12.54, 0.29, 0.68, 1.11 and 85.37%, as shown in Fig. 4c–i, which revealed the uniform distribution of O, S, Cd, Cr and Zn in the synthesized CdSQDs@ZnCr-LDO/ZnO nanocomposite, thereby increasing the number of available adsorption.[24]

Furthermore, the high-resolution transmission electron microscopic (HR-TEM) images and selective area electron diffraction (SAED) patterns of ZnO NPs, CdSQDs, ZnCr-LDO NSs, and CdSQDs@ZnCr-LDO/ZnO nanocomposite are shown in Fig. 5a–h. The diffraction fringes of (111) and (220) planes of crystalline ZnO NPs can be clearly observed, as shown in Fig. 5b, with interplanar line spacings of 0.30 and 0.33 nm, respectively. Furthermore, Fig. 5c and d suggests the successful synthesis of polycrystalline CdSQDs with noticeable particle size of 3–10 nm. In addition, the well-dispersion and anchoring of CdSQDs onto ZnCr-LDO NPs in the ternary nanocomposite is apparent across all corners and layers of the created sheets of ZnCr-LDO matrix over ZnO NPs surfaces, as illustrated in Fig. 5g. Additionally, the average particle size of the ternary nanocomposite was about 37 nm in harmony with the XRD findings.

3.4 Structural properties

To conduct a more in-depth evaluation of the surface chemical composition and elemental oxidation states of the as-fabricated CdSQDs@ZnCr-LDO/ZnO nanocomposite, X-ray photoelectron

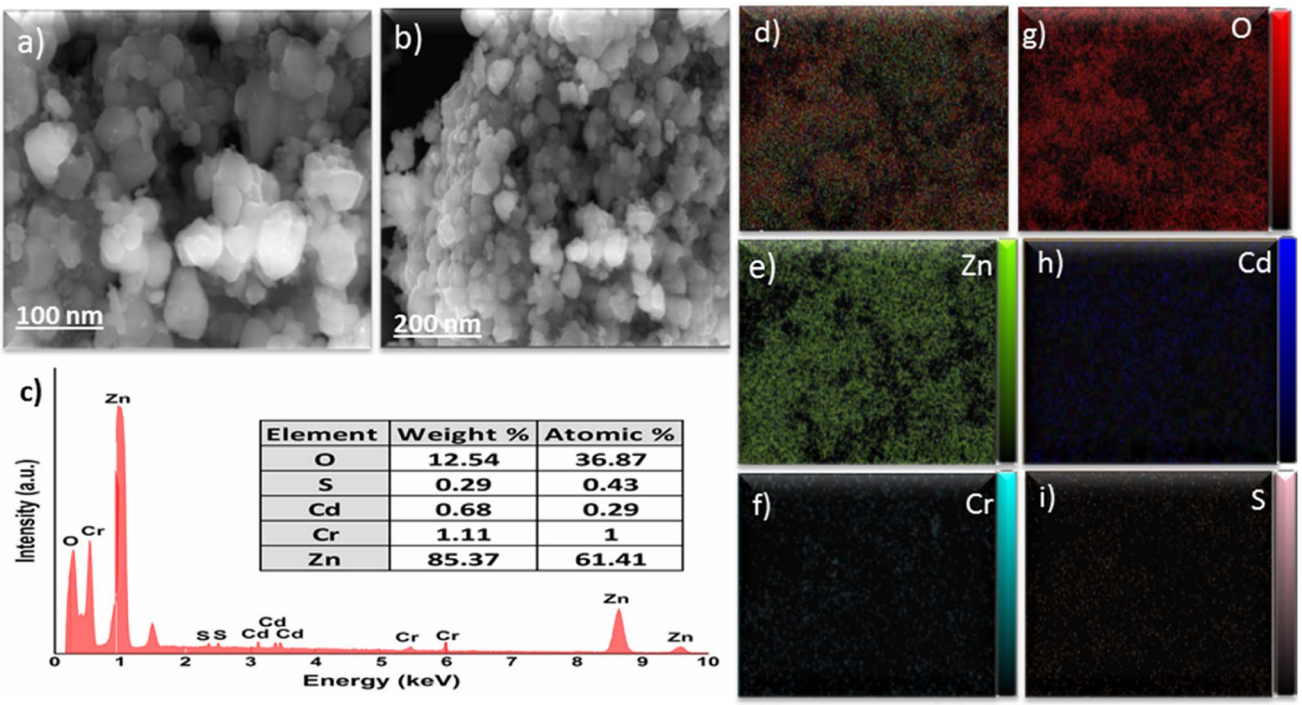

Fig. 4 Scanning electron microscopic images of (a) CdSQDs@ZnCr-LDO/ZnO nanocomposite and (b) EDX mapping for CdSQDs@ZnCr-LDO/ZnO nanocomposite (c and d) elemental overlay for CdSQDs@ZnCr-LDO/ZnO nanocomposite and (e–i) the spectral mapping of each element in CdSQDs@ZnCr-LDO/ZnO.

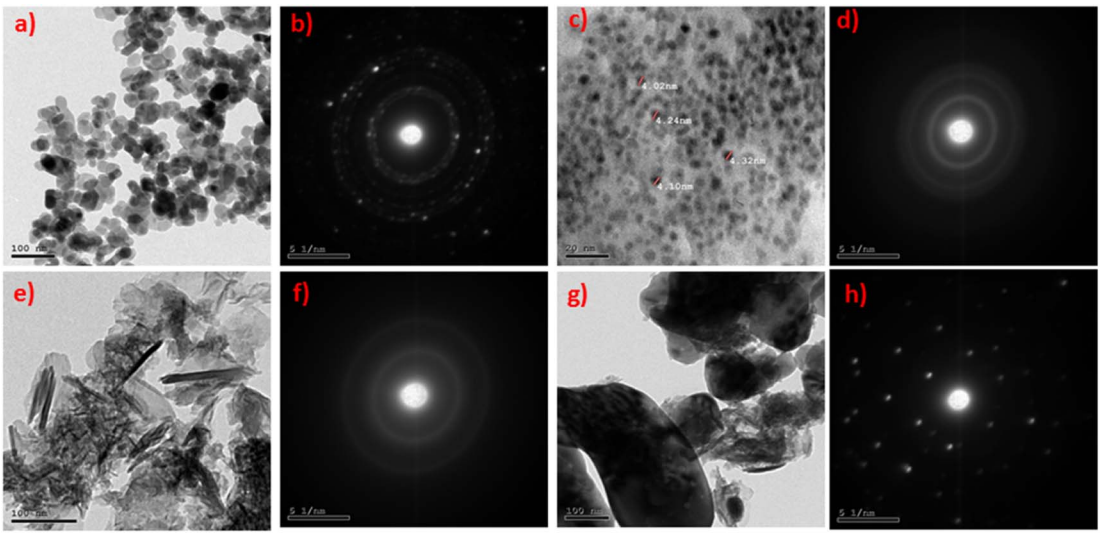

Fig. 5 The HR-TEM images and the corresponding SAED patterns of (a and b) ZnO NPs, (c and d) CdSQDs, (e and f) ZnCr-LDO nanosheet, and (g and h) CdSQDs@ZnCr-LDO/ZnO ternary nanocomposite.

spectroscopy (XPS) was used, as shown in Fig. 6a–f. The obtained spectra revealed the presence of Cd, S, Cr, Zn, and O elements on the surfaces of the prepared ternary nanocomposite, with corresponding peaks around 412.28, 161.88, 586.18, 1045.28 and 530.78 eV, respectively. Moreover, the full survey narrow-scan spectrum of the individual elements are displayed in Fig. 6a. Two main strong peaks of Cd positioned at 405.58 eV and 412.28 are referring to the binding energies (BE) of Cd $3d_{5/2}$ and Cd $3d_{3/2}$, as demonstrated in Fig. 6b, in harmony with previously reported data.[25] Furthermore, the O (1s) spectrum, shown in Fig. 6e, exhibited three BE components congruous low binding energy (LBE), middle binding energy

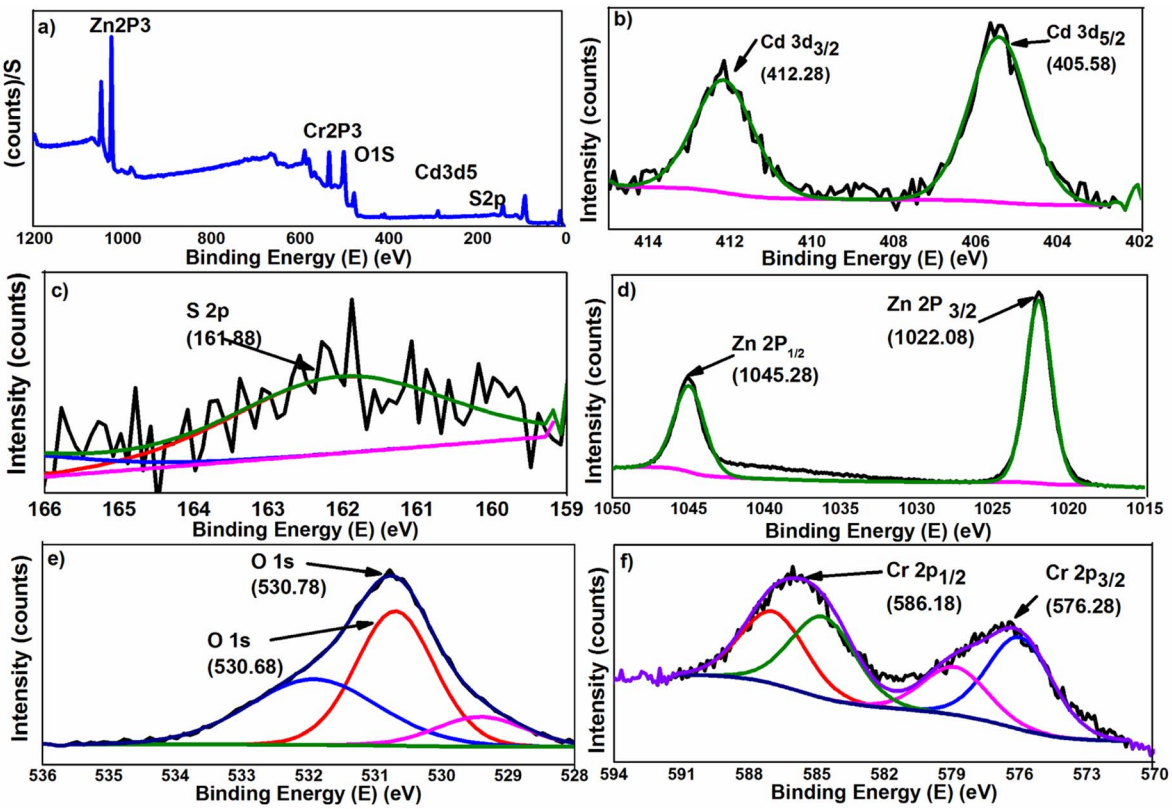

Fig. 6 (a) Sample survey XPS spectrum of CdSQDs@ZnCr-LDO/ZnO, High resolution XPS spectra of (b) Cd (3d), (c) S (2p), (d) Zn (2p), (e) O (1s), and (f) Cr (2p).

(Mid-BE), and high binding energy (HBE), corresponding to 529.38, 530.78, and 532.08 eV peaks, respectively, similar to previously reported data.[15] The LBE was ascribed to O^{2-} ions at the essential sites of bonding between Zn^{2+} ions and O^{2-} ions in the hexagonal ZnO structure and the Mid-BE was ascribed to the O^{2-} ions in the imperfect oxygen region. While the HBE emission spectrum was attributed to the chemisorbed oxygen vacancies.[9,26] Moreover, the peak profiles of Zn spectrum was deconvoluted into 2 main peaks, as illustrated in Fig. 6d, at 1022.08 eV and 1045.28 eV that are associated with Zn $2p_{3/2}$ and Zn $2p_{1/2}$, respectively, with peaks matched to Zn atom at the disciplinarian lattice sites in ZnO NPs.[27] Furthermore, the disparity in binding energies (BE) between the Zn $2p_{3/2}$ and Zn $2p_{1/2}$ peaks was determined to be 23.2 eV, indicative of the characteristic value for the hexagonal Wurtzite ZnO NPs structure.[24] Compared with ZnCr-LDO, the binding energies (BE) of Cr 2p and Zn 2p in CdSQDs@ZnCr-LDO/ZnO show an obviously negative shift. Conversely, the binding energies (BE) of Cd $3d_{3/2}$, Cd $3d_{5/2}$ and S 2p in CdSQDs@ZnCr-LDO/ZnO display explicit shift to high energy values, compared with native pecursors. These obvious shifts are characteristic of the bonding and hybridization between the ZnCr-LDO nanosheets and the CdSQDs, which involves the electron transfer from CdSQDs to ZnCr-LDO. The results reveals the existence of strong electronic interaction between the CdSQDs and ZnCr-LDO nanosheets over ZnO surfaces in such a heterostructure, that is valuable to diminish the photoinduced charges and carriers recombination throughout the photocatalytic process.

3.5 Textural analysis

Brunauer–Emmett–Teller (BET) surface area analysis and Barrett–Joyner–Halenda (BJH) pore size and volume analysis were conducted to study the textural characteristics of the CdSQDs@ZnCr-LDO/ZnO nanocomposite, as illustrated in Fig. 7a. The N_2 adsorption–desorption isotherms at 77 K, Fig. 7a, is categorized as type IV with an H3 hysteresis loop following IUPAC classifications (observed within the pressure range of 0.85–0.95 P/P_0), and that is characteristic for slits-like pores structure.[26] The determined specific surface area of the synthesized CdSQDs@ZnCr-LDO/ZnO ternary nanocomposite was 90.90 $m^2\ g^{-1}$, with an average diameter of 48 nm. The nanocomposite exhibited a consistent pore size distribution, indicating the existence of a monomodal *meso*-porosity (Fig. 7b). The obtained BET surface area of the as-synthesized ternary nanocomposite exceeds those previously reported for pure ZnO nanoparticles (64.2 $m^2\ g^{-1}$) and CdS/ZnO composite (23.76 $m^2\ g^{-1}$).[25] The greater surface area, in this work, is likely due to the 2D layered structure of the ZnCr-LDO NSs and the uniform dispersion of ultra-small CdSQDs throughout the nanocomposite structure.

The high surface area of 90.9 $m^2\ g^{-1}$ provided more active sites for both dye molecules adsorption and active radicals generation. Moreover, the large surface area led to faster diffusion and mass transfer of reactive species, causing improved photocatalytic reaction kinetics. Also, more dye molecules adsorption likely occurred on the high surface area nanostructure before and during irradiation. Overall, the large surface area of the as-prepared ternary nanocomposite contributed significantly to its excellent performance in RhB dye removal.

3.6 Zeta potential measurements

Zeta potential, serving as a measurable indicator of electrostatic interactions among particles, plays a crucial role in evaluating the stability of nanoparticles. Precise assessments of zeta potential provide valuable insights into the determinants of

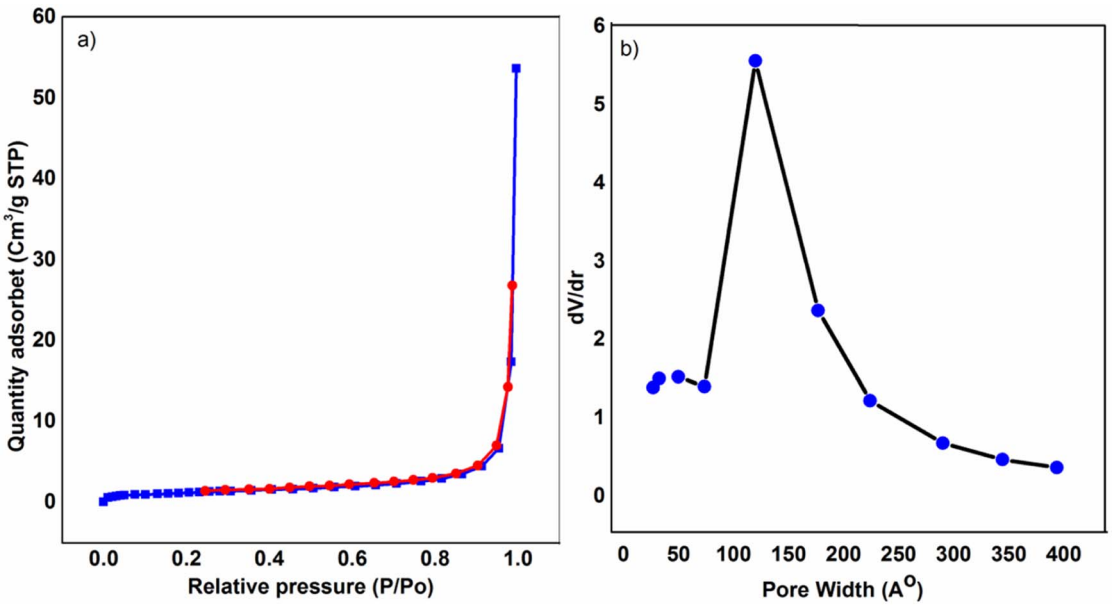

Fig. 7 (a) Nitrogen adsorption/desorption isotherm of CdSQDs@ZnCr-LDO/ZnO nanocomposite (b) pore size distribution according to BJH analysis.

particle dispersion, aggregation, and clumping. This enables the refinement of formulations for dispersions, emulsions, and suspensions. In the specific case of the CdSQDs@ZnCr-LDO/ZnO nanocomposite, the scattering of 0.10 g of the nanocomposite in 10 mL of distilled water yielded a positive zeta potential of 0.128 mV, indicative of electrostatic stability. This observation aligns with the determined pH_{pzc} (point of zero charge) of the CdSQDs@ZnCr-LDO/ZnO nanocomposite, recorded at 6.50. Understanding the interplay between solution pH, the pH_{pzc}, and the pK_a of RhB is essential for comprehending the catalytic process. Rhodamine B has a pK_a of about 4.2 corresponding to the dissociation of the aromatic carboxylic group. When the solution pH falls between 4.20 and 6.50, the ternary nanocomposite catalyst has positively charged surfaces that enhance the adsorption of the negatively charged carboxylate moieties of RhB molecules, potentially improving the catalytic performance. Conversely, at pH levels surpassing 6.50, the pH_{pzc}, the negatively charged catalyst surface may influence interactions with RhB, potentially diminishing its catalytic efficiency. The consideration of pH in relation to the pK_a of RhB is crucial, since it influences the charge status of the dye molecules, thereby diminishing their interaction with the catalyst.[13]

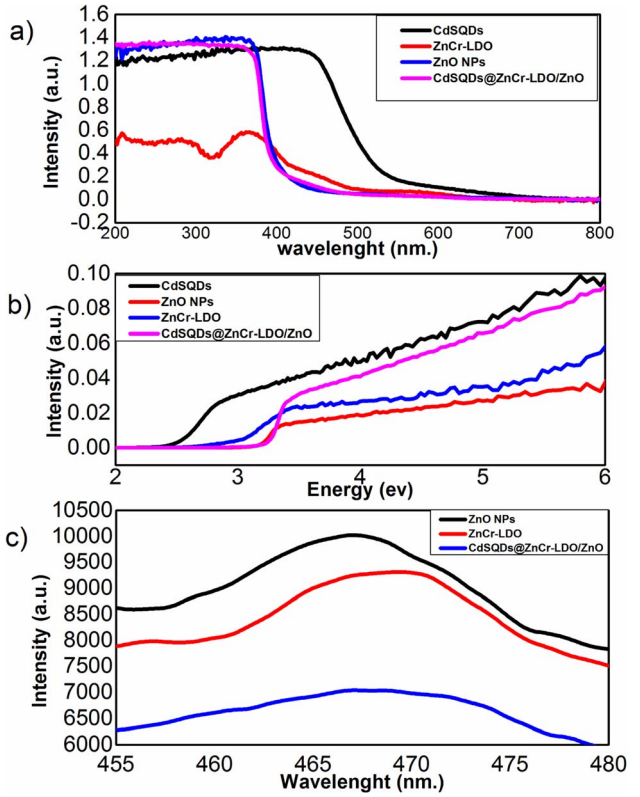

Fig. 8 (a) DRS spectra, (b) Tauc plots, and (c) PL spectra of the as-fabricated nanomaterials (ZnO NPs, ZnCr-LDO, CdSQDs@ZnCr-LDO/ZnO).

3.7 Optical properties

3.7.1 UV-vis DRS analysis and band structure determination. The UV–vis diffuse reflectance spectroscopy (DRS) was utilized to examine the optical properties, and the BE of the as-fabricated CdSQDs@ZnCr-LDO/ZnO, as shown in Fig. 8a. The distinct absorptions are observed at 544, 405, and 485 nm for CdSQDs, ZnO NPs, and ZnCr-LDO individual samples, respectively. The existence of the absorption maximum at 395 nm confirms the development of the hexagonal wurtzite phase in the structure of ZnO NPs, showcasing a well-defined crystalline lattice nature.[28] The DRS data and Kubelka–Munk (K–M) model[29,30] has been employed to evaluate the bandgap energy (BE) of the as-fabricated samples from their spectral data, Fig. 8b. The estimated bandgap energy values, listed in Table 1, were 2.2, 2.7, 3.2 and 3.1 eV for CdSQDs, ZnCr-LDO, ZnO and CdSQDs@ZnCr-LDO/ZnO samples, respectively, which were in harmony with previously reported values.[31]

These results revealed that the as-fabricated nanocomposite sample absorbs extra photo energy (visible/UV-A light) than its individual components indicating its efficacy in solar light harvesting. The similarity in the UV-vis absorption spectra between ZnO NPs and the CdSQDs@ZnCr-LDO/ZnO nanocomposite can be attributed to the high weight percentage (90%) and strong absorption characteristics of the ZnO NPs present in the ternary nanocomposite. Additionally, the presence of CdSQDs (1 wt%) and ZnCr-LDO nanosheets (9 wt%) in the ternary composite does not significantly alter the overall absorption spectrum, which is still dominated by the ZnO NPs 90% fraction.

3.7.2 Photoluminescence spectral analysis. Room temperature-photoluminescence (PL) spectral measurements were conducted to investigate the luminescence characteristics and evaluate the electron–hole (e–h) pair recombination

Table 1 The estimated band-gap energies (E_g), average crystallite size (D) of the prepared ternary CdSQDs@ZnCr-LDO/ZnO nanocomposites and its precursors for RhB dye removal

			RhB removal% (pH = 6.0, 1×10^{-5} mol L^{-1} RhB, 0.10 g L^{-1} catalyst, 150 min)			
Catalyst	D (nm)	E_g (eV)	(Dak)	(2 Fluorescent white lamps)	(UV-A lamp)	Photocatalysis rate constant, k min^{-1}
ZnO	40	3.2	11.0	34.1	38.02	0.002041
CdSQDs	3.7	2.2	—	—	—	—
ZnCr-LDO	40.8	2.7	17.0	30.6	40.2	0.00147
CdSQDs@ZnCr-LDO/ZnO	58	3.1	15.8	50.4	98.03	0.02158

behavior of the as-prepared samples, Fig. 8c, where broad emission peaks were obtained in the wavelength range of 455–480 nm with maximum originated at 467 nm for the pristine ZnO NPs sample. These emission peaks are due to the recombination of photoinduced electrons in CB with corresponding photoinduced holes in VB.[2,32] The as-fabricated ZnO NPs peak photoluminescence intensity signifies an exceptionally rapid electron–hole recombination rate. After incorporation of CdSQDs and ZnCr-LDO onto the surfaces of ZnO NPs, the exhibited quenching of PL intensity was attributed to its slight shift in the main emission peaks. The as-fabricated ternary nanocomposite CdSQDs@ZnCr-LDO/ZnO sample, however, had the lowest electron–hole recombination rate when compared to the as-fabricated ZnO sample. This can be attributed to the contribution of free electrons from CdSQDs (donor) to ZnO NPs (acceptor), which entails the quick generation of photogenerated electron–holes as well as the low rate of recombination. This provided the as-fabricated CdSQDs@ZnCr-LDO/ZnO nanocomposite with superior photocatalytic performance as compared to its individual precursor photocatalysts, which is useful for increasing the efficiency of solar (visible/UV-A) light harvesting.

4. Catalytic performance of CdSQDs@ZnCr-LDO/ZnO in RhB degradation

The RhB photocatalytic degradation was monitored under UV-A irradiation while using the as-fabricated CdSQDs@ZnCr-LDO/ZnO nanocomposite as a promising catalyst. Changes in the RhB concentration C/C_o were obtained at maximum absorbance (A/A_o, λ = 554 nm). Fig. 9a shows the excellent efficacy of the synthesized CdSQDs@ZnCr-LDO/ZnO nanocomposite in RhB dye photocatalytic degradation under UV-A light source where exceptional discoloration was acquired in 150 min. The discoloration of RhB dye was accompanied by a progressive hypsochromic effect, as seen by a decrease in bands intensities at 262, 293, 312, and 355 nm in the UV region (not shown for simplicity), until all visible and UV peaks vanished after 150 minutes of UV-A exposure. These findings confirm the photodegradation of chromogenic centers as well as disintegration of the aromatic rings of RhB dye structure and signify the conversion of RhB dye into H_2O and CO_2 through mineralization[13,33]

It is important to note that after 150 minutes, the RhB dye removal% increased from 15.8 in the dark to 50.4% under two fluorescent white lamps, but to 98% under the used UV-A lamp, as shown in Fig. 9a, b and Table 1.

4.1 The kinetics of RhB photodegradation

The photodegradation process encompasses chemical reactions occurring under UV-A irradiation. Thus, kinetics becomes essential to evaluate the efficiency of the fabricated CdSQDs@ZnCr-LDO/ZnO nanocomposite in RhB photodegradation, hence the order of reaction (n) and rate constant (k) were evaluated.

Fig. 10a–c represent the zero-, pseudo-first (PFO) and second-order kinetic plots, respectively. The PFO kinetic plot exhibited better fitting to a linear relationship with absolute correlation coefficient (R^2) of 0.99936 indicating that the photocatalytic performance of the prepared CdSQDs@ZnCr-LDO/ZnO obeys the pseudo-first-order kinetics. The non-linear nature of Fig. 10a and c plots indicates that the current photocatalytic reaction does not follow zero or second-order kinetics. Furthermore, by employing the differential method, the R^2 of the depicted plot in Fig. 10d was determined to be 0.9999, signifying that the photocatalytic reaction obeys first-order kinetics. Besides, the curve's slope in Fig. 10e is found to be zero, indicating that the reaction conforms to pseudo-first-order kinetics. All these observations collectively suggest that the photodegradation of RhB facilitated by the CdSQDs@ZnCr-LDO/ZnO nanocomposite obeys first-order kinetics.

4.2 Factors affecting RhB dye photocatalytic degradation efficiency using CdSQDs@ZnCr-LDO/ZnO nanocomposite

The RhB photocatalytic degradation was optimized by studying various experimental parameters including the as-fabricated

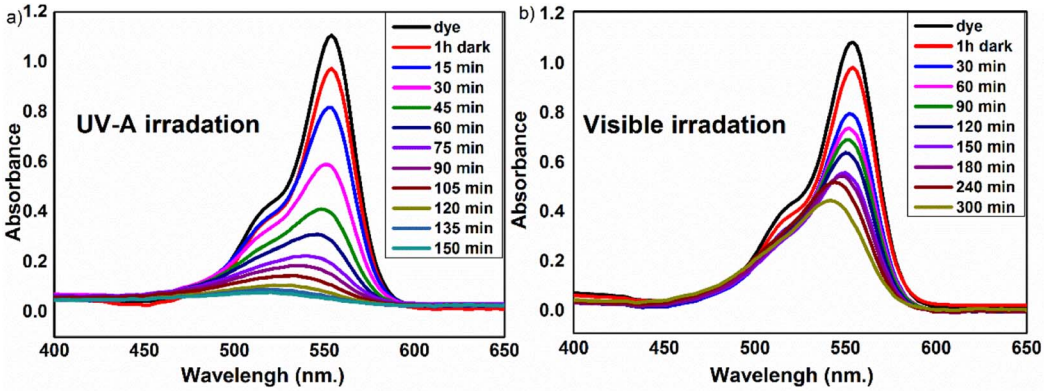

Fig. 9 Time-dependent progress of RhB photodegradation using the CdSQDs@ZnCr-LDO/ZnO ternary nanocomposites under (a) UV-A irradiation, and (b) fluorescent white light; ([catalyst] = 0.10 g L^{-1}, initial RhB concentration $[RhB]_o = 1 \times 10^{-5}$ M, and pH = 6.0 at room temperature of 25 °C).

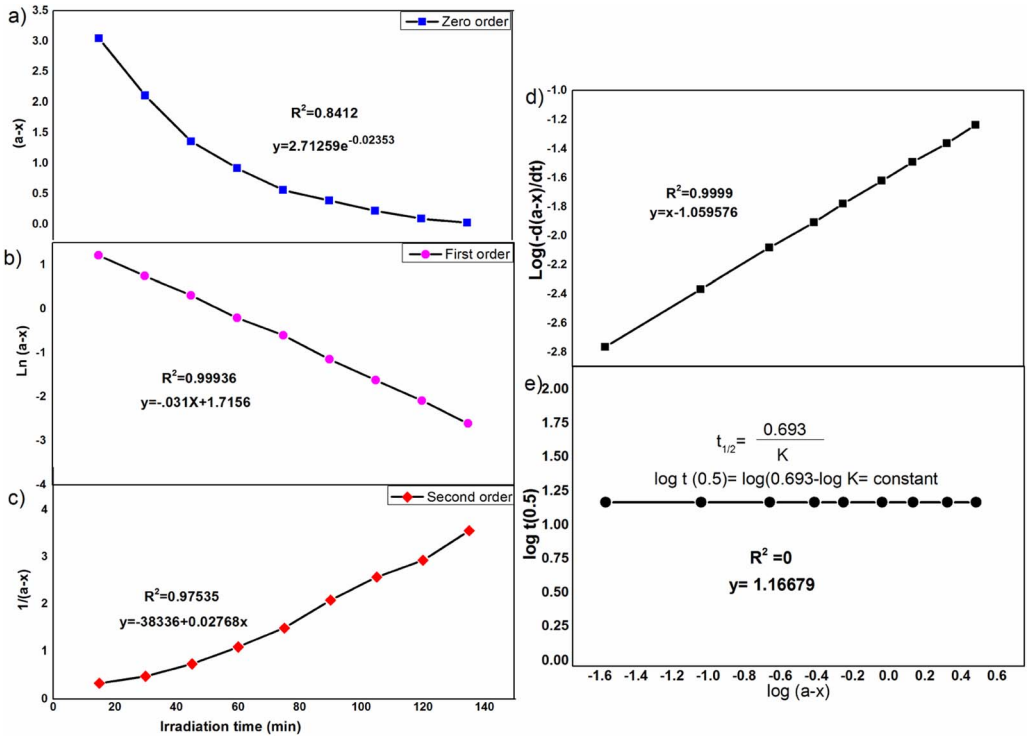

Fig. 10 Graphical representation to obtain the order of the RhB degradation using the as-synthesized ternary CdSQDs@ZnCr-LDO/ZnO nanocomposites using (a) the graphical method, (b) the differential method, and (c) the $t_{0.5}$ method [RhB] = 1×10^{-5} M, [catalyst] = 0.10 g L^{-1}, and the pH value = 6.0.

CdSQDs@ZnCr-LDO/ZnO wt% composition, medium pH (2.0–10.0), UV-A irradiation time (0–150 min), catalyst dose (0.05–0.17 g L^{-1}), and the initial RhB dye concentration (0.5–1.5 × 10^{-5} mol L^{-1}), as shown in Fig. 11a–c.

4.2.1 Effect of irradiation time. Contact time is regarded as one of the most crucial parameters that obviously affect the photodegradation efficiency of a dye. Thus, the RhB dye photodegradation catalyzed by CdSQDs@ZnCr-LDO/ZnO ternary nanocomposite was investigated under UV-A irradiation for 0–150 min. A 100 mL of 5.0 mg L^{-1} aqueous RhB dye solution containing 0.10 g L^{-1} catalyst was adjusted to a pH of 6.0. The reacting mixture was stirred at 700 rpm in a dark box for 60 min to allow adsorption/desorption equilibrium, before switching on the UV-A lamp. As shown in Fig. 9a and b when RhB solution was stirred with the CdSQDs@ZnCr-LDO/ZnO ternary nanocomposite (in the dark), there was a 15.8% decline in RhB color within the first 60 minutes, but there was no further decline for the next 2 hours of stirring, indicating the occurrence of the adsorption/desorption equilibrium. After that time, it is apparent that RhB dye photocatalytic degradation's rate raised regularly with increasing the UV-A radiation time, where a maximum RhB dye removal was achieved after 150 min, during which the incident UV-A light energy on the photocatalyst's surfaces increased the chances of producing photoexcited species, thereby increasing the photocatalytic efficiency.

4.2.2 Effect of CdSQDs@ZnCr-LDO/ZnO photocatalyst dose. The effect of catalyst dose (0.05 to 0.17 g L^{-1}) on the photodegradation of 1×10^{-5} mol L^{-1} RhB at pH 6.0 was investigated, as shown in Fig. 11a and Table 2. The RhB photodegradation% rose upon increasing the photocatalyst dose from 0.05 to 0.10 g L^{-1}, due to the abundance of the photocatalyst's active sites relative to the constant concentration of $[RhB]_o$. However, increasing the photocatalyst dose from 0.10 to 0.17 g L^{-1} caused a slight decline in RhB photodegradation% as more photocatalyst loading blocked some active sites on the catalyst surfaces and slightly distracted incident UV-A light due to the abundance of dispersed catalyst NPs. This behavior is consistent with earlier reports.[13,34]

4.2.3 Influence of the initial RhB concentration. The impact of various initial RhB dye concentrations (0.5–1.5 × 10^{-5} mol L^{-1}) on the performance of CdSQDs@ZnCr-LDO/ZnO photocatalyst was studied, as shown in Fig. 11b and Table 2 that revealed a noticeable dependence of photodegradation% and photocatalytic reaction rate on the initial $[RhB]_o$ concentration. The RhB dye photocatalytic degradation% decreased from 99.18 to 94.09% by increasing the initial RhB dye concentration from 0.5×10^{-5} to 1.5×10^{-5} mol L^{-1}, which can be partly ascribed to a decrease in the number of photons reaching the photocatalyst's surface active sites due to increased light absorption by the increased abundance of dye molecules. Additionally, the higher RhB concentration forms an inner-filter that hinders the falling light owing to increasing the solution opacity in addition to blocking the active accessible sites on CdSQDs@ZnCr-LDO/ZnO catalyst.[35]

4.2.4 Influence of the medium pH. The pH significantly influences both the adsorption and photocatalytic degradation

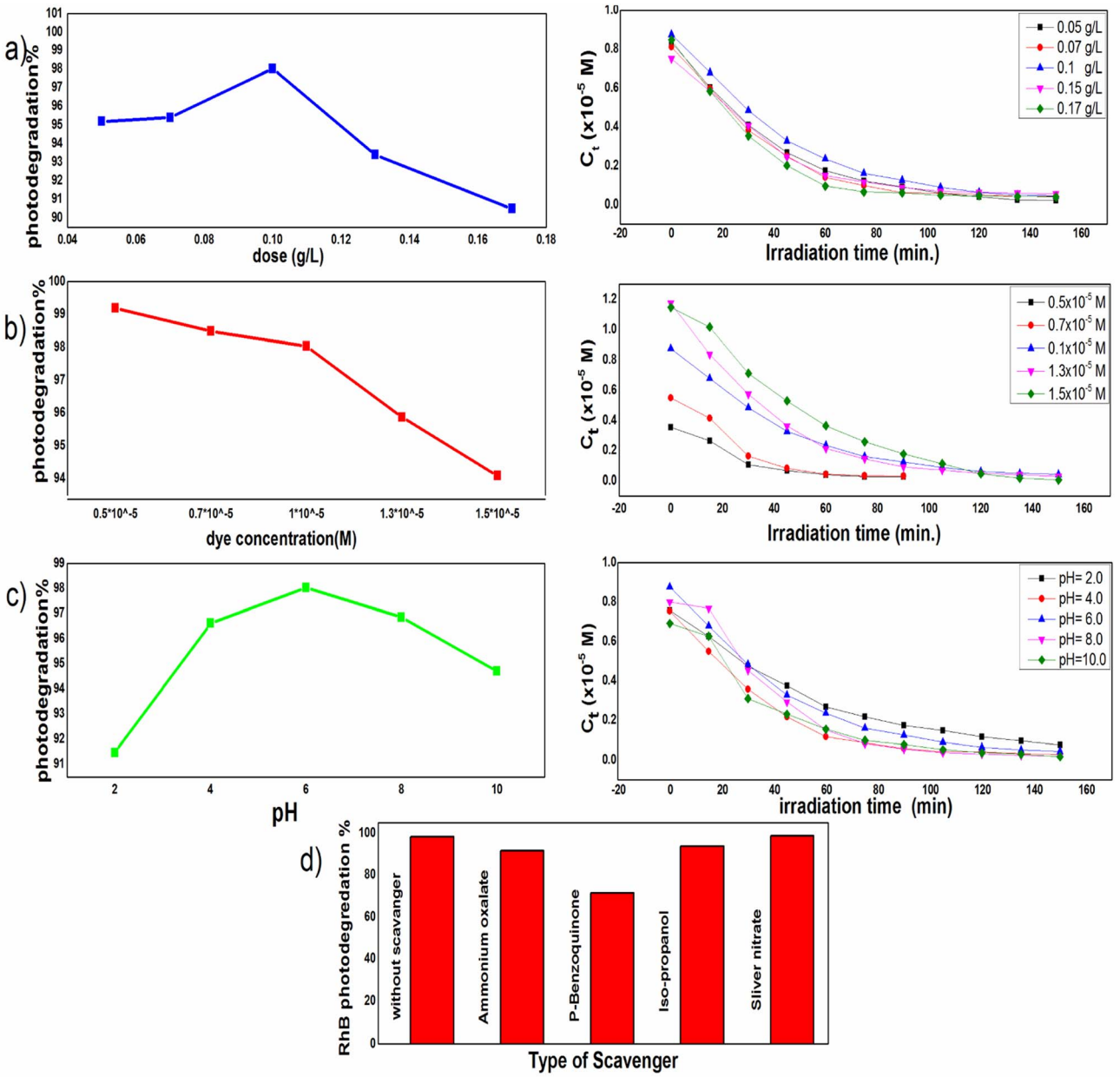

Fig. 11 Effects of (a) catalyst dose, (b) RhB dye concentration, (c) medium pH and (d) scavenger's type on RhB photocatalytic degradation catalyzed by CdSQDs@ZnCr-LDO/ZnO ternary nanocomposites, following the recommended procedure.

processes, as it affects the photocatalyst's surface charges, valence band [VB] oxidation potential, adsorption, some intrinsic physicochemical characteristics and generation active sites on catalyst surfaces, mainly due to various protolytic equilibria.[2,36] The photodegradation of RhB dye catalyzed by CdSQDs@ZnCr-LDO/ZnO ternary nanocomposite was studied as function in the range of pH 2.0–10.0, as shown in Fig. 11c and Table 2, while keeping other parameters constant. Dilute NaOH or HCl solutions were used to adjust the solution pH of the stirred dye solution containing the photocatalyst. The results revealed that optimum performance as achieved at pH = 6.0 ± 0.5; by increasing the pH from 6.0 to 10.0, the dye degradation% decreased from 98.4 to 90.7%. This is partly attributed to various protolytic equilibria involving the formation of less reactive RhB molecules and catalyst surfaces;[2,37] *e.g.*, the formation of RhB zwitterions that produce bulky less reactive dimeric forms. On the other hand, at low pH values, the photocatalytic degradation rate decreased partly due to the generation of less reactive oxygen species, as well as the formation of RhB cations that repulse with positively charged catalyst's surface active sites, resulting in decreased photodegradation%.[2,38]

4.2.5 The role of reactive species. The RhB photocatalytic degradation catalyzed by the as-fabricated CdSQDs@ZnCr-LDO/ZnO nanocomposites was investigated to evaluate the reactive species responsible for the catalytic effect. Several scavenging

Table 2 Effects of various parameters influencing RhB photocatalytic degradation in the presence of the as-fabricated CdSQDs@ZnCr-LDO/ZnO ternary nanocomposite

[Catalyst] (g L^{-1})	$[RhB]_o$ (mol L^{-1})	pH	RhB photodegradation%	k_{abs} (min^{-1})
0.05	1.0×10^{-5}	6.0	95.18	0.0392
0.07	1.0×10^{-5}	6.0	95.39	0.0472
0.10	1.0×10^{-5}	6.0	98.03	0.0365
0.15	1.0×10^{-5}	6.0	93.38	0.0419
0.17	1.0×10^{-5}	6.0	90.48	0.0434
0.10	0.5×10^{-5}	6.0	99.18	0.0644
0.10	0.7×10^{-5}	6.0	98.49	0.0782
0.10	1.3×10^{-5}	6.0	95.87	0.0368
1.0	1.5×10^{-5}	6.0	94.09	0.0332
0.10	1.0×10^{-5}	2.0	91.47	0.026
0.10	1.0×10^{-5}	4.0	96.61	0.0383
0.10	1.0×10^{-5}	8.0	96.85	0.0413
0.10	1.0×10^{-5}	10.0	94.70	0.0309

reagents such as *p*-benzoquinone (PQ), sliver nitrate, ammonium oxalate and isopropanol were employed to trap $^{\bullet}O_2^-$, $^-e_{cb}$, $^+h_{vb}$, and $^{\bullet}OH$, respectively,[39,40] where the scavenger's concentration was fixed to (1×10^{-5} mol L^{-1}), as shown in Fig. 11d. The use of benzoquinone, isopropanol, ammonium oxalate and silver nitrate as $^{\bullet}O_2^-$, $^{\bullet}OH$, $^-e_{cb}$, and $^+h_{vb}$ scavengers resulted in 40.45, 4.0, 8.0 and 1.0% reduction in the RhB photodegradation%, respectively, as shown in Fig. 11d. Therefore, the superoxide radical was the most contributing reactive oxygen species in RhB photocatalytic degradation catalyzed by the as-prepared CdSQDs@ ZnCr-LDO/ZnO photocatalyst.

5. Proposed mechanism of RhB photocatalytic degradation

5.1 The overarching mechanism of photocatalysis

The overarching RhB dye photocatalytic degradation mechanism by a semiconductors-based photocatalyst can be described by eqn (1)–(12). Generally, a photocatalytic reaction initiates upon exposure to incident photons, resulting in the generation and acceleration of photo-induced electrons (e_{CB}^-). This occurs through the transfer and excitation of electrons from the valence band (VB) to the conduction band (CB), leaving positive holes (h_{VB}^+) in the VB (eqn (1)). The generated holes (h_{VB}^+) can degrade RhB dye molecules directly *via* oxidation (eqn (2)) or *via* the generation of $^{\bullet}OH$ that further oxidize the dye molecules, as shown in eqn (3) and (4). Conversely, the (e_{CB}^-) is capable of degrading organic dye pollutants either *via* a direct reductive pathway (eqn (5)) or indirectly by producing ($O_2^{\bullet-}$) (eqn (6)), which can further participate in RhB degadation (eqn (7)). Therefore, the generated reactive species h_{VB}^+, $O_2^{\bullet-}$, e_{CB}^- and $OH^{\bullet}$ are the basis of RhB photocatalytic degradation process. However, the possible recombination of generated electron–hole pairs (e_{CB}^- and h_{VB}^+) adversely reduce the entire photocatalytic process, eqn (8).

$$\text{Semiconductor} \xrightarrow{h\nu} \text{Semiconductor} + (e_{CB}^- + h_{VB}^-) \quad (1)$$

$$h_{VB}^+ + \text{RhB} \rightarrow \text{Degradation products} \quad (2)$$

$$h_{VB}^+ + H_2O \rightarrow OH^{\bullet} \quad (3)$$

$$OH^{\bullet} + \text{RhB} \rightarrow \text{Degradation products} \quad (4)$$

$$e_{CB}^- + \text{RhB} \rightarrow \text{Degradation products} \quad (5)$$

$$e_{CB}^- + O_2 \rightarrow O_2^{\bullet-} \quad (6)$$

$$O_2^{\bullet-} + \text{RhB} \rightarrow \text{RhB}^{\bullet-} \rightarrow \text{Degradation yields} \quad (7)$$

$$e_{CB}^- + h_{VB}^+ \rightarrow h\nu \text{ or heat} \quad (8)$$

5.2 The proposed RhB dye photocatalytic degradation mechanism

The primary factor contributing to the low photocatalytic efficiency observed in the degradation of RhB by pristine ZnO NPs or ZnCr-LDO NSs is the rapid recombination rate of electron–hole pairs, as illustrated in Fig. 10. While there was a hypothesis that the two-dimensional coupling semiconductor in the binary nanocomposites might improve the separation of electron–hole pairs compared to their individual counterparts, this relies on having compatible band alignments between the binary semiconductors. Consequently, the energy levels of the conduction band (CB) and valence band (VB) relative to the standard hydrogen electrode (NHE), along with the corresponding positions of these energy bands for both binary and ternary nanocomposites, were calculated. These computations were determined using the evaluated optical band gap energies (E_g) and their associated values of electronegativity (EN), as outlined in eqn (9)–(12).

$$E_{CB} = X - 4.5 - \frac{1}{2}E_g \quad (9)$$

$$E_{VB} = X - 4.5 + \frac{1}{2}E_g \quad (10)$$

$$X = \frac{1}{2}(E_{EA} + E_{ion}) \quad (11)$$

$$E_{VB} = E_{CB} + E_g \quad (12)$$

where E_{CB} and E_{VB} denote the edge potentials of the (CB) and (VB) of the semiconductor, respectively. The symbol "X" signifies the Mulliken's absolute electronegativity (EN) values of the semiconductor; ("X" = 5.27, 5.76, and 6.63 for CdSQDs, ZnO NPs, and ZnCr-LDO NSs, respectively[32]), E_g represents the quantified bandgap energy in electron volts (eV), and the energy possessed by the free electron E_e (4.5 eV *vs.* NHE). The calculated E_{CB} values were −0.26, −0.41 and −1.06 eV for ZnO, CdSQDs and ZnC-LDO NSs, respectively, while, the calculated E_{VB} values were 2.34, 1.79 and +1.64 eV for ZnO, CdSQDs and ZnC-LDO NSs, respectively. Composite semiconductors can enhance the photocatalytic activity *via* appropriate band alignment. For instance, the excited electron in the CB has the ability to independently convey energy from the CB of the 1st semiconductor to the lower CB of the 2nd semiconductor. As a result, the "h_{vB}^{+}" holes can spontaneously migrate towards the elevated valence band of the 2nd semiconductor. This aligns with eqn (13); illustrating the noted synergistic impact in the binary composite of CdSQDs@ZnO that is credited to the establishment of a "type II heterojunction". This suggested scenario, depicted in Fig. 12, is anticipated to enhance the separation of electron–hole pairs, consequently enhancing the photocatalytic effectiveness of the binary nanocomposites, as inferred from PL measurements.

$$\mathrm{CdSQDs@ZnO} \rightarrow \mathrm{CdSQDs}(e_1^- + h_1^+) + \mathrm{ZnO}(e_2^- + h_2^+) \rightarrow \mathrm{CdSQDs}(e_1^- + e_2^- + h_1^+) + \mathrm{ZnO}(e_2^- + h_1^+ + h_2^+) \quad (13)$$

Fig. 12 illustrates the envisioned mechanism underlying the photocatalytic efficiency of the as-synthesized CdSQDs@ZnCr-LDO/ZnO ternary nanocomposite, employing various strategies to enhance the likelihood and facilitate the injection of electrons e_{CB}^- into alternative conduction bands, thereby minimizing e–hole recombination. The CB of ZnO is anticipated to be the primary CB housing electrons, given its elevated energy level in contrast to ZnO and ZnCr-LDO. Conversely, the VB of CdSQDs is anticipated to be the uppermost conduction band with positive holes (h^+), given its diminished energy level compared to those of ZnCr-LDO and CdSQDs. Thus, eqn (14) reflects synergistic enhancements stemming from the formation of three type II heterojunctions within every separate binary nanocomposite. This proposition aligns with the substantial reduction in the electron–hole recombination rate suggested by earlier PL measurements for CdSQDs@ZnCr-LDO/ZnO.

$$\mathrm{CdSQDs@ZnCr\text{-}LDO} \xrightarrow[\mathrm{ZnO}]{h\nu} \mathrm{CdSQDs}(e_{CB}^- + h_{VB}^+) + \mathrm{ZnO}(e_{CB}^- + h_{VB}^+) + \mathrm{ZnCr\text{-}LDO}(e_{CB}^- + h_{VB}^+) \rightarrow \mathrm{CdSQDs}(e_1^- + h_1^+ + h_2^+ + h_3^+) + \mathrm{ZnCr\text{-}LDO}(e_1^- + e_2^- + h_2^+ + h_3^+) + \mathrm{ZnO}(e_3^- + e_2^- + e_1^- + h_3^+) \quad (14)$$

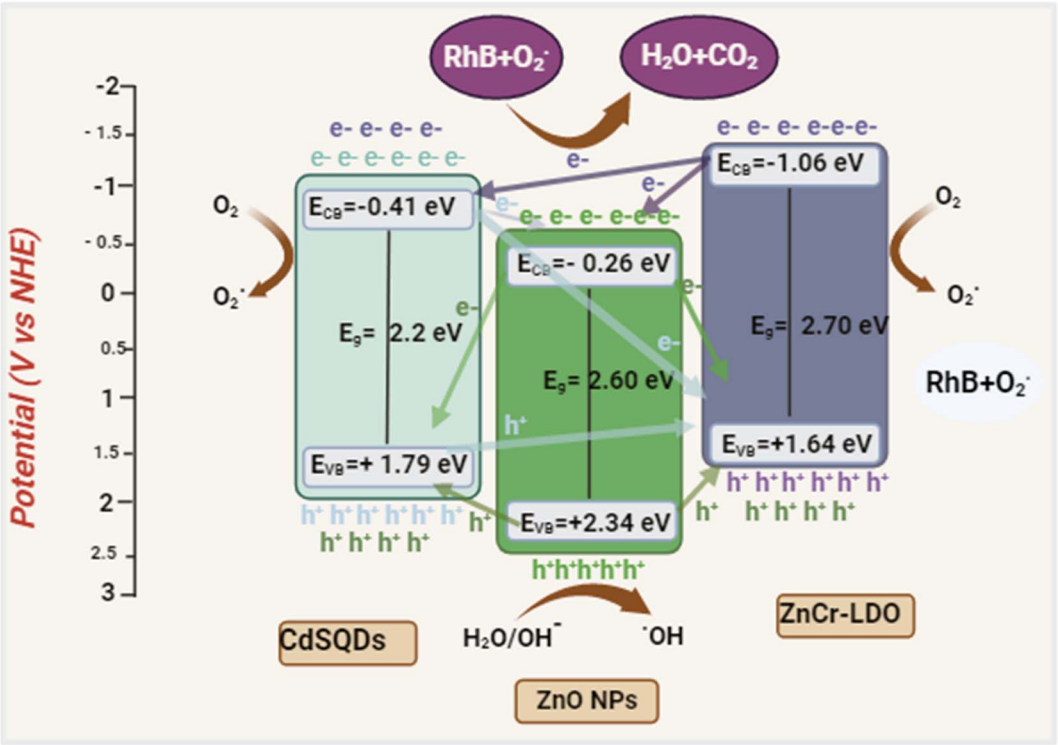

Fig. 12 Z-scheme type II heterojunction mechanism for the enhanced photocatalytic activity of the CdSQDs@ZnCr-LDO/ZnO ternary nanocomposite.

Besides, the strategic configuration of the band structure in the ternary CdSQDs@ZnCr-LDO/ZnO nanocomposite is devised to amplify the likelihood of establishing Z-scheme heterojunctions. This promotes the movement of electrons (e_{CB}^-) from the CB of one semiconductor to the VB of the other two semiconductors, ensuring the improved separation of charges and the enhanced overall photocatalytic performance *via* multiple type II Z-scheme heterojunctions. These findings collectively highlight the remarkable photocatalytic efficacy and the envisaged synergistic performance of the CdSQDs@ZnCr-LDO/ZnO ternary nanocomposite when compared to its individual components or binary counterparts.

Table 3 Comparison between the as-fabricated CdSQDs@ ZnCr-LDO/ZnO ternary nanocomposite photocatalytic activity towards RhB photodegradation with previously reported data

Catalyst	Light source	Period	$[RhB]_o$ (M)	[Catalyst] (g L^{-1})	Removal%	Ref.
ZnO	300 W Xe lamp	480 min	5×10^{-5}	NA	58%	41
CdS/ZnO	300 W Xe lamp	480 min	5×10^{-5}	NA	85%	41
CdS/ZnO	1000 W halogen lamp	180 min	1×10^{-5}	1.0	90%	42
CdS	300 W filament lamp	120 min	1×10^{-5}	1.0	37%	43
10% CdS@ZnO/g-C_3N_4	15 W UV-A lamp	120 min	1×10^{-5}	1.0	93.3%	44
Zn–Cr–CO_3 LDH	Solar light irradiation	180 min	1×10^{-5}	1.0	15%	36
10%CdSQDs@ZnO	15 W UV-A lamp	120 min	1×10^{-5}	1.0	18%	32
ZnO/CdS/TiO_2	350 W Xe lamp	120 min	1×10^{-5}	—	90%	45
5% g-C_3N_4/ZnO	500 W Xe lamp	100 min	1×10^{-5}	2	97%	46
ZnO	20 W UV-A lamp	150 min	1×10^{-5}	0.10	38.02%	Current work
CdSQDs/ZnO					46.7%	
ZnCr-LDO					40.2%	
CdSQDs/ZnCr-LDO					62.3%	
ZnCr-LDO/ZnO					76.5%	
CdSQDs@ZnCr-LDO/ZnO					98.03%	

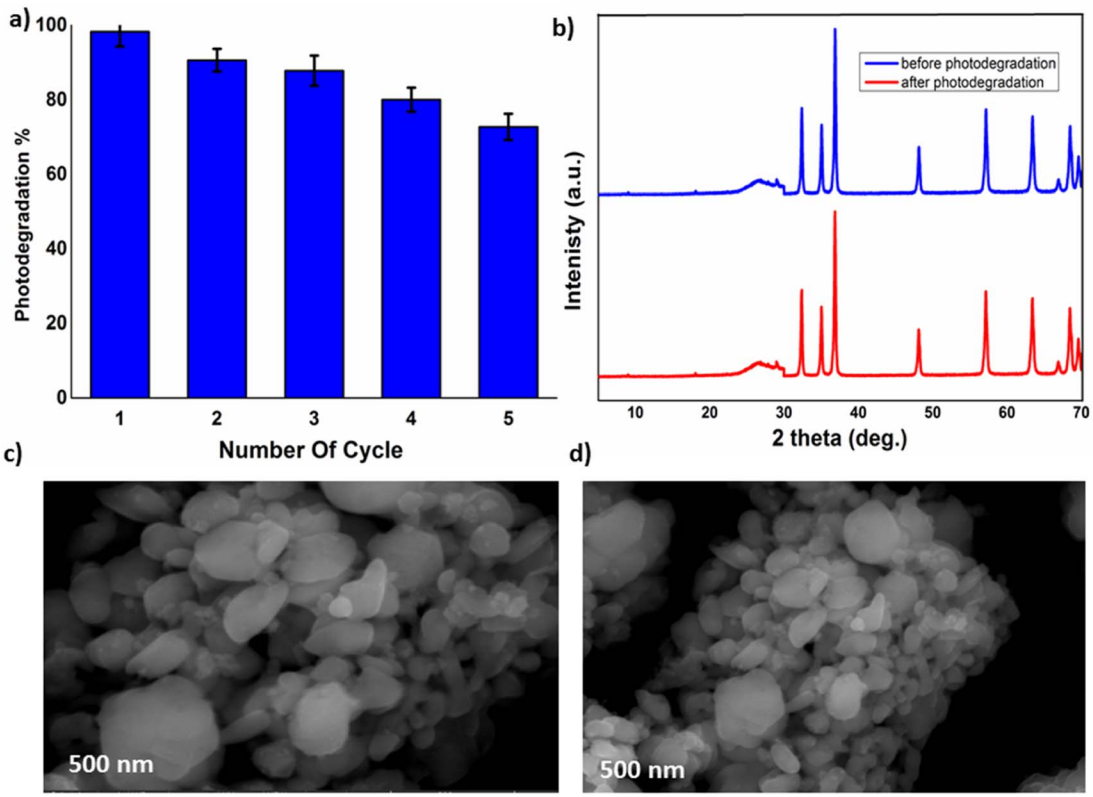

Fig. 13 (a) Reusability and recyclability study of the as-fabricated CdSQDs@ZnCr-LDO/ZnO on the photocatalytic efficiency in RhB photodegradation. (b) XRD patterns of native and recycled catalyst after photodegradation process, (c and d) FE-SEM images of native and recycled catalyst, respectively.

5.3 Comparison with previous reports

The as prepared CdSQDs@ZnCr-LDO/ZnO catalyst efficacy in the photocatalytic degradation of RhB dye as a model organic pollutant was compared with previously reported data of some relevant photocatalysts, as shown in Table 3. The advantages of as-fabricated CdSQDs@ZnCr-LDO/ZnO include the quantitative dye degradation, the low-intensity lamps (20 W), the shorter irradiation time, the wide operating pH range matching real wastewaters, and the low catalyst dosage.

5.4 Photostability, reusability & recyclability of CdSQDs@ZnCr-LDO/ZnO catalyst

For practical implementation and catalyst reuse, it is crucial to assess the stability, efficacy, and recyclability of the as-fabricated nanocomposite catalyst. To investigate the catalyst's photostability and photoactivity, the spent photocatalyst was collected, washed with ethanol after each cycle, filtered, dried, sieved, and reused again. Fig. 13a shows the results of five consecutive RhB degradation cycles using the recovered CdSQDs@ZnCr-LDO/ZnO catalyst. Data revealed that the photocatalytic efficacy decreased only slightly over the course of five consecutive cycles, so that even after five experimental cycles, the photocatalyst retained 80% of its reactivity, confirming its great stability. The slight decrease in efficacy is partly attributed to blockage, deterioration, or collapse of some active centers on the photocatalyst surfaces. Furthermore, Fig. 13b depicts the XRD patterns of native and recycled catalysts, demonstrating the presence of all phases of CdSQDs, ZnO NPs, and ZnCr-LDO NSs in both samples with no discernible shift in peak positions or crystalline size, albeit with slightly reduced intensity of some peaks. Furthermore, Fig. 13c and d display FESEM images of native and recycled catalyst samples, which have identical morphology and a uniform distribution of CdSQDs and ZnO NPs over ZnCr-LDO NSs. These findings support the photocatalyst's stability, chemical resistance, long-term durability, and potential for repeated usage in wastewater treatment.

6. Conclusions

In this work, CdSQDs@ZnCr-LDO/ZnO ternary nanocomposite was successfully synthesized *via* a facile and simple method for the highly effective photocatalytic degradation of RhB dye under 20 W UV-A light irradiation. Physicochemical characterization tools, including XRD, SEM, HTEM, FTIR, EDS, XPS, DRS, and PL analysis confirmed the composition, nanostructure and important characteristics of the as-prepared nanocomposite catalyst. Findings of PL and scavengers studies confirmed that superoxide, hydroxyl radicals and positive holes were the essential reactive species for photodegradation RhB dye. The as-prepared nanocomposite preserved its efficacy over five consecutive cycles of regeneration and reuse. Comparison with previously reported photocatalysts showed the high efficacy of the as-prepared ternary nanocomposite even at low catalyst dose, low wattage lamp requirement and short irradiation times.

Conflicts of interest

There is no conflict of interest.

References

1 M. Adel, M. A. Ahmed, M. A. Elabiad and A. A. Mohamed, Removal of heavy metals and dyes from wastewater using graphene oxide-based nanomaterials: A critical review, *Environ. Nanotechnol., Monit. Manage.*, 2022, **18**, 100719.
2 M. A. Ahmed and A. A. Mohamed, Recent progress in semiconductor/graphene photocatalysts: synthesis, photocatalytic applications, and challenges, *RSC Adv.*, 2023, **13**(1), 421–439.
3 M. A. Ahmed and A. A. Mohamed, A systematic review of layered double hydroxide-based materials for environmental remediation of heavy metals and dye pollutants, *Inorg. Chem. Commun.*, 2023, **148**, 110325.
4 M. A. Ahmed, M. A. Ahmed and A. A. Mohamed, Facile adsorptive removal of dyes and heavy metals from wastewaters using magnetic nanocomposite of zinc ferrite@ reduced graphene oxide, *Inorg. Chem. Commun.*, 2022, **144**, 109912.
5 J. Di, *et al.*, Electrochemical activation combined with advanced oxidation on $NiCo_2O_4$ nanoarray electrode for decomposition of Rhodamine B, *J. Water Proc. Eng.*, 2020, **37**, 101386.
6 J. Wang, *et al.*, Insights into the efficient adsorption of rhodamine B on tunable organo-vermiculites, *J. Hazard Mater.*, 2019, **366**, 501–511.
7 B.-J. Bie, *et al.*, Dextran Fluorescent Probes Containing Sulfadiazine and Rhodamine B Groups, *Molecules*, 2022, **27**(19), 6747.
8 P. Amornpitoksuk and S. Suwanboon, Comparative study of the photocatalytic decolorization of rhodamine B dye by AgI-Ag_3PO_4 prepared from co-precipitation and ion-exchange methods, *J. Alloys Compd.*, 2017, **720**, 582–588.
9 S. Khamparia and D. Jaspal, Investigation of adsorption of Rhodamine B onto a natural adsorbent Argemone mexicana, *J. Environ. Manage.*, 2016, **183**(Part 3), 786–793.
10 B. S. Shagolsem and N. M. Singh, Green synthesis and magnetically separable Fe_3O_4/SnO_2/g-C_3N_4 ternary nanocomposite for degradation of Rhodamine B, *Inorg. Chem. Commun.*, 2024, **160**, 111877.
11 M. Sakar, R. Mithun Prakash and T.-O. Do, Insights into the TiO_2-based photocatalytic systems and their mechanisms, *Catalysts*, 2019, **9**(8), 680.
12 H. Yaghoubi, *et al.*, Toward a visible light-driven photocatalyst: the effect of midgap-states-induced energy gap of undoped TiO_2 nanoparticles, *ACS Catal.*, 2015, **5**(1), 327–335.
13 M. A. Ahmed and A. A. Mohamed, Advances in ultrasound-assisted synthesis of photocatalysts and sonophotocatalytic processes: A review, *iScience*, 2023, **27**, 108583.
14 H. Zhang, *et al.*, Switching on wide visible light photocatalytic activity over $Mg_4Ta_2O_9$ by nitrogen doping for water oxidation and reduction, *J. Catal.*, 2019, **377**, 455–464.

15 Y. Guo, *et al.*, Photocatalytic activity enhanced *via* surface hybridization, *Carbon Energy*, 2020, **2**(3), 308–349.
16 M. A. Ahmed, A. A. Brick and A. A. Mohamed, An efficient adsorption of indigo carmine dye from aqueous solution on mesoporous Mg/Fe layered double hydroxide nanoparticles prepared by controlled sol-gel route, *Chemosphere*, 2017, **174**, 280–288.
17 G. Zhang, *et al.*, Layered double hydroxides-based photocatalysts and visible-light driven photodegradation of organic pollutants: A review, *Chem. Eng. J.*, 2020, **392**, 123684.
18 M. Xu and M. Wei, Layered double hydroxide-based catalysts: recent advances in preparation, structure, and applications, *Adv. Funct. Mater.*, 2018, **28**(47), 1802943.
19 S. Kundu and M. K. Naskar, Carbon-layered double hydroxide nanocomposite for efficient removal of inorganic and organic based water contaminants–unravelling the adsorption mechanism, *Mater. Adv.*, 2021, **2**(11), 3600–3612.
20 P. Yazdani, *et al.*, Layered double hydroxide nanoparticles as an appealing nanoparticle in gene/plasmid and drug delivery system in C_2C_{12} myoblast cells, *Artif. Cells, Nanomed., Biotechnol.*, 2019, **47**(1), 436–442.
21 W. Jin and D.-H. Park, Functional layered double hydroxide nanohybrids for biomedical imaging, *Nanomaterials*, 2019, **9**(10), 1404.
22 A. A. Shalaby and A. A. Mohamed, Determination of acid dissociation constants of Alizarin Red S, Methyl Orange, Bromothymol Blue and Bromophenol Blue using a digital camera, *RSC Adv.*, 2020, **10**(19), 11311–11316.
23 E. M. Hashem, *et al.*, Novel Z-Scheme/Type-II CdS@ ZnO/g-C_3N_4 ternary nanocomposites for the durable photodegradation of organics: Kinetic and mechanistic insights, *Chemosphere*, 2021, **277**, 128730.
24 B. S. Shagolsem and N. M. Singh, Ternary photocatalyst of Fe_3O_4/Ag-SnO_2 with Parkia speciosa extract improves visible-light-driven photocatalytic degradation of dye, *Inorg. Chem. Commun.*, 2024, 112245.
25 S. Wang, *et al.*, One-step synthesis of water-soluble CdS quantum dots for silver-ion detection, *ACS Omega*, 2021, **6**(10), 7139–7146.
26 S. K. Pandey, *et al.*, Effect of growth temperature on structural, electrical and optical properties of dual ion beam sputtered ZnO thin films, *J. Mater. Sci.: Mater. Electron.*, 2013, **24**, 2541–2547.
27 Y. Naciri, *et al.*, Preparation, characterization and photocatalytic degradation of Rhodamine B dye over a novel $Zn_3(PO_4)_2$/BiPO4 catalyst, *J. Environ. Chem. Eng.*, 2019, **7**(3), 103075.
28 M. Pudukudy, *et al.*, Facile synthesis of bimodal mesoporous spinel Co_3O_4 nanomaterials and their structural properties, *Superlattices Microstruct.*, 2013, **64**, 15–26.
29 Z. Li, *et al.*, NiS_2/reduced graphene oxide nanocomposites for efficient dye-sensitized solar cells, *J. Phys. Chem. C*, 2013, **117**(13), 6561–6566.
30 M. Parthibavarman, *et al.*, High visible light-driven photocatalytic activity of large surface area Cu doped SnO_2 nanorods synthesized by novel one-step microwave irradiation method, *J. Iran. Chem. Soc.*, 2018, **15**(12), 2789–2801.
31 S. Padmanathan and A. Prakasam, Design and fabrication of hybrid carbon dots/titanium dioxide (CDs/TiO_2) photoelectrodes for highly efficient dye-sensitized solar cells, *J. Mater. Sci.: Mater. Electron.*, 2020, **31**(4), 3492–3499.
32 A. Akhundi and A. Habibi-Yangjeh, Ternary g-C_3N_4/ZnO/AgCl nanocomposites: synergistic collaboration on visible-light-driven activity in photodegradation of an organic pollutant, *Appl. Surf. Sci.*, 2015, **358**, 261–269.
33 S. Padmanathan and A. Prakasam, Incorporation of carbon dots on the ZnO Nanosheets as metal–organic framework Photoanodes for high efficient dye sensitized solar cell applications, *J. Cluster Sci.*, 2021, **32**(4), 795–804.
34 B. Cuiping, *et al.*, Removal of rhodamine B by ozone-based advanced oxidation process, *Desalination*, 2011, **278**(1–3), 84–90.
35 M. Abdellah, *et al.*, Photocatalytic decolorization of methylene blue using TiO_2/UV system enhanced by air sparging, *Alexandria Eng. J.*, 2018, **57**(4), 3727–3735.
36 W. Liu, *et al.*, Facile synthesis of g-C_3N_4/ZnO composite with enhanced visible light photooxidation and photoreduction properties, *Chem. Eng. J.*, 2012, **209**, 386–393.
37 K. Sathiyan, *et al.*, Controllable synthesis of TiO_2 nanoparticles and their photocatalytic activity in dye degradation, *Mater. Res. Bull.*, 2020, **126**, 110842.
38 M. Ahmed, *et al.*, Effect of porphyrin on photocatalytic activity of TiO_2 nanoparticles toward Rhodamine B photodegradation, *J. Photochem. Photobiol., B*, 2017, **176**, 25–35.
39 M. Umar and H. A. Aziz, Photocatalytic degradation of organic pollutants in water, *Organic pollutants-monitoring, risk and treatment*, 2013, vol. 8, pp. 196–197.
40 Z. Abou-Gamra, M. Ahmed and M. A. Hamza, Investigation of commercial $PbCrO_4$/TiO_2 for photodegradation of rhodamine B in aqueous solution by visible light, *Nanotechnol. Environ. Eng.*, 2017, **2**, 1–10.
41 T. Fujita, *et al.*, Free radical degradation in aqueous solution by blowing hydrogen and carbon dioxide nanobubbles, *Sci. Rep.*, 2021, **11**(1), 3068.
42 K. A. Adegoke, *et al.*, Synthesis, characterization and application of CdS/ZnO nanorod heterostructure for the photodegradation of Rhodamine B dye, *Mater. Sci. Energy Technol.*, 2019, **2**(2), 329–336.
43 Y. Xu and W. D. Zhang, CdS/g-C_3N_4 hybrids with improved photostability and visible light photocatalytic activity, *Eur. J. Inorg. Chem.*, 2015, **2015**(10), 1744–1751.
44 T. Jana, A. Pal and K. Chatterjee, Self assembled flower like CdS–ZnO nanocomposite and its photo catalytic activity, *J. Alloys Compd.*, 2014, **583**, 510–515.
45 E. M. Hashem, M. A. Ahmed and M. F. Abdel Messih, Facile one-pot aqueous synthesis of highly soluble and luminescent CdSe quantum dots without nitrogen bubbling, *CrystEngComm*, 2020, **22**, 4816–4822.
46 A.-Y. Zhang, *et al.*, Degradation of refractory pollutants under solar light irradiation by a robust and self-protected ZnO/CdS/TiO_2 hybrid photocatalyst, *Water Res.*, 2016, **92**, 78–86.